FeN_4 active sites generated on dipyridylpyridazine functionalized reduced graphene oxide for high-performance air electrode in a Zn-air battery.

Juan Amaro-Gahete,[a‡] Valentín García-Caballero,[b‡] Almudena Benítez,[c*] Dolores G. Gil-Gavilán,[a] R. Rojas-Luna,[a] Dolores Esquivel,[a] Antonio J. Fernández-Romero,[d] Manuel Cano,[b*] Juan J. Giner-Casares,[b] Francisco J. Romero-Salguero,[a*]

[a]*Departamento de Química Orgánica, Instituto Químico para la Energía y el Medioambiente (IQUEMA), Facultad de Ciencias, Universidad de Córdoba, Campus de Rabanales, Edificio Marie Curie, E-14071 Córdoba, Spain.*

[b]*Departamento Química Física y Termodinámica Aplicada, IQUEMA, Facultad de Ciencias, Universidad de Córdoba, Campus de Rabanales, Edificio Marie Curie, E-14071 Córdoba, Spain.*

[c]*Departamento Química Inorgánica e Ingeniería Química, IQUEMA, Facultad de Ciencias, Universidad de Córdoba, Campus de Rabanales, Edificio Marie Curie, E-14071 Córdoba, Spain.*

[d]*Grupo de Materiales Avanzados para la Producción y Almacenamiento de Energía, Universidad Politécnica de Cartagena, Aulario II, Campus de Alfonso XIII, 30203 Cartagena, Spain.*

*Corresponding authors: *q02rosaf@uco.es*, *q82calum@uco.es*, *q62betoa@uco.es*

‡ These authors contributed equally to this work

Abstract

The growing global electricity demand requires the development of cost-effective energy conversion and storage systems, integrating inexpensive, eco-friendly, and high-efficiency catalysts. Oxygen reduction reaction (ORR) is considered crucial process to achieve high-power-density fuel cells and Zn-air batteries (ZABs). The latter have attracted the attention of scientific community due to its high theoretical energy density, reliable safety and low-cost. However, several limitations must be overcome, designing ORR catalysts thought versatile and economical synthetic routes. In this sense, the non-noble iron-nitrogen-carbon materials (Fe-N-C) have been reported as the most potential candidates for attaining superior activity toward ORR in substitution of the high-priced commercial Pt-C catalysts. Herein, Diels-Alder surface adducts based on dipyridylpyridazine units have been created along 2D surface of reduced graphene oxide (rGO) nanosheets for the controlled generation of FeN_4 active sites at the edges through successive solvent-free mechanochemical reactions and an additional thermal treatment. The optimized catalyst provided high content of pyridinic-N, graphitic-N and Fe^{2+} species, contributing to the excellent activity delivered as electrocatalyst for ORR processes. In addition, a flooded ZAB assembled with this material as cathodic/air electrode exhibited an excellent specific capacity of 141.1 $A \cdot h \cdot g^{-1}$, improving the catalytic performance obtained for the 10 wt.% Pt-C benchmark electrocatalyst.

Keywords: Reduced graphene oxide; Diels-Alder functionalization; FeN_4 active site; oxygen reduction reaction; Zn-air battery.

1. Introduction

The world is facing an urgent need to transition from fossil fuel-based energy systems towards more sustainable, and efficient energy sources [1–4]. Electrochemical devices have emerged as promising alternatives to satisfy the growing global energetic demand and mitigate the climate change reducing carbon emissions [5–8]. Over the recent years, significant efforts have been made to implement a wide range of actions to advance this cause. Notably, there has been a strong focus on the development of electric vehicles, with considerable progress made in terms of technological advancements and widespread adoption [9–11]. Furthermore, clean energy storage systems have been introduced, seamlessly integrating intermittent solar/wind energy sources with electrochemical energy storage technologies, providing a reliable and sustainable solution for the efficient utilization of renewable energy [12,13]. The collective implementation of these initiatives represents a crucial step forward in achieving a more environmentally friendly and sustainable energy landscape. Among them, metal-air batteries and fuel cells have garnered considerable attention due to their high energy density, ample resource availability, impressive energy storage efficiency, integration with renewable energy sources, decentralized power generation, viability of electric transportation at zero-emissions, long durability and great flexibility and scalability [14–18]. Prominent examples include proton exchange membrane fuel cells (PEMFCs) [19], hydrogen fuel cells [20], direct methanol fuel cells (DMFCs) [21], molten-carbonate fuel cells (MCFCs) [22], solid oxide fuel cells (SOFCs) [23], zinc-air batteries [24], aluminum-air batteries [25], iron-air batteries [26], lithium-air batteries [27], and sodium-air batteries [28], among others.

Specifically, the Zn-air batteries (ZABs) have acquired significant attention as a prospective system for next-generation energy storage devices due to its exceptional safety, abundant resources, and high theoretical energy density (1086 W h kg^{-1}) to name only a few [29–31]. Its versatility extends to various potential application fields, including electric vehicles, distributed energy storage, flexible wearable electronics and microcurrent devices [32,33]. However, efforts are underway to address some limitations related with the slow recharge rate, cycle life, size and weight of the batteries, sensitivity to environmental conditions, and overall usability [34]. Ongoing research focuses on optimizing electrode designs, enhancing cycling stability, and developing new materials and electrolyte solutions to overcome these challenges [35–40]. Generally, ZABs use zinc as anode and oxygen from the air as cathode [41]. Regarding the oxygen reduction

reaction (ORR) carried out in the positive electrode, certain constraints are currently addressed [42–45], comprising: i) slow reaction kinetics leading to higher polarization losses and reduced power output; ii) the high cost, degradation and low availability of precious metal catalysts (i.e., platinum); iii) mass transport limitations to drive the efficient diffusion of reactants (oxygen) and products (water) to and from the catalyst surface; and iv) carbonation of the electrolyte due to reaction of carbon dioxide present in the air with the alkaline electrolyte. Thus, the diligent exploration of alternative materials functioning as cathode catalysts is of paramount importance in the pursuit of achieving enhanced sustainability, economic impact and performance in Zn-air energy systems [46].

Single-atoms FeN_4 sites on carbon-based materials have garnered significant attention as highly efficient catalysts for the ORR in ZABs [47]. Whilst carbon supports provide excellent electrical conductivity, high surface area, remarkable stability and flexibility for the introduction of heteroatoms such as nitrogen [48], the FeN_4 active sites offer several important advantages, including exceptional catalytic activity, enhanced selectivity, and improved durability [49–54]. More specifically, nitrogen-based functional groups integrated into the graphitic substrate also have a crucial impact on the effectiveness and electron conductivity of ORR electrocatalysis [55–57]. Pyridinic-N, for instance, promotes a more favourable onset potential, while graphitic-N significantly enhances the maximum current density achievable during ORR [58–60]. Additionally, the presence of pyridinic-N groups facilitates the coordination of Fe atoms, resulting in the formation of FeN_4 bridging structures [61,62]. This, in combination with the synergistic effect of active graphitic-N functional groups, further improves the O_2 and CO_2 electroreduction performance [63].

The synthesis of such carbon-based materials primarily relies on two distinct approaches: the template-sacrifice method involving metal-organic frameworks [64–66] or silica support [67,68], and the integration of FeN_4 active sites within a carbon matrix like carbon nanotubes, graphene or activated carbon [69–72]. These procedures are based on simultaneously heat-treating of iron salts, N-containing organic compounds and carbon supports at high temperature giving rise to the generation of unpredictable N-type sites. In addition, computational studies have demonstrated the key role of isolated FeN_4 sites located at the edge superior to the one in plane in graphitic-like structures in the resulting electrocatalytic properties [73,74]. In this sense, our group has corroborated this analysis preparing atomically dispersed FeN_4 coordinated to surface dipyridilpyridazine Diels-

Alder adducts situated at the edges of 3D multilayer graphene matrix by novel low-temperature and solvent-free mechanochemical synthesis [75]. The material subjected to thermal treatment at 240 ºC under nitrogen atmosphere exhibited an unprecedented electrocatalytic behaviour for ORR, considering this strategy a potential approach for the production of efficient and low-cost electrocatalyst materials for renewable energy technologies (metal-air batteries, water splitting or fuel cells).

Herein, we have extended the scope of our previous study using graphene oxide (GO) as conducting support, which is a very interesting carbon-based material. GO contains multiple available functional groups (such as alcohol, ether, epoxide, and carboxylic acid) as well as is easily disperse in water, being highly processable. A solvent-free mechanochemical reactions assisted by ball milling have been carried out for the generation of Diels-Alder surface adducts of dipyridylpyridazine on the graphene sheets and the subsequent coordination of iron atoms forming FeN_4 active sites. In addition, this material has shown excellent performance for ORR electrocatalysis and the application in a real energy storage device such as ZABs. Hence, the findings have demonstrated that this synthetic methodology can be expanded to encompass additional 2D substrates based on graphene.

2. Experimental Section

2.1. Chemicals and Materials

Graphite powder extra fine (**GP**), potassium permanganate ($KMnO_4$, ACS reagent, ≥99.0%), hydrogen peroxide (H_2O_2, 30% (w/w) in H_2O, contains stabilizer), 2-pyridinecarbonitrile ($C_6H_4N_2$, 99%), hydrazine hydrate (reagent grade, N_2H_4 50-60 %), acetic acid (CH_3COOH, ReagentPlus, ≥99.99%), sodium nitrite ($NaNO_3$, ACS reagent, ≥97.0%), 2,3-dichloro-5,6-dicyano-p-benzoquinone (DDQ, 98%) and sulfuric acid (H_2SO_4, ACS reagent, 95.0-98.0%) were purchased from Sigma Aldrich. Iron (III) nitrate nonahydrate pure ($Fe(NO_3)_3 \cdot 9H_2O$, 98%), nitric acid (HNO_3, 69%) and hydrochloric Acid (HCl, 37%) was obtained from PanReac, AppliChem ITW reagents. Dichloromethane (CH_2Cl_2, anhydrous, ≥99.8%, contains 40-150 ppm amylene as stabilizer), chloroform ($CHCl_3$, anhydrous, ≥99%, contains 0.5-1.0% ethanol as stabilizer) and ethanol were purchased from Labbox Labware S.L. All the reagents and solvents were used as received without further purification. Graphene oxide (**GO**) was prepared following the modified Hummers method described in a previous research [76].

3,6-Di(2-pyridyl)-1,2,4,5-tetrazine (**dptz**) was synthesized by a previously reported procedure [77].

2.2. Synthesis of materials

2.2.1. Synthesis of rGO-dppz

The rGO-dppz material was prepared following a modified synthetic methodology based on Diels-Alder reactions between dptz units and different graphene-derived materials [75,78]. Then, 2 g of GO and 0.5 g (2 mmol) of dptz were reacted into a planetary ball mill (Retsch PM100, Retsch GmbH, Haan, Germany) under dry conditions at 600 rpm with reversal of rotation every 30 min during 24 h. The excess of unreacted dptz in the resulting solid was removed by washing successively with 150 mL of CH_2Cl_2, three times at room temperature and two twice at 40 ºC. After that, the material was dried at 120 °C under vacuum overnight. Subsequently, an aromatization process was carried out with DDQ as dehydrogenation agent using a weight ratio of 4:1 solid:DDQ in 150 mL of $CHCl_3$ for 24 h at room temperature. After washing many times with $CHCl_3$ by successive redispersions to eliminate excess of DDQ, the resulting material named **rGO-dppz** was dried at 120 °C under vacuum overnight.

2.2.2. Synthesis of rGO-dppz@Fe

A dry ball milling process (Retsch PM100, Retsch GmbH, Haan, Germany) was employed for the reaction of 2 g of rGO-dppz with an excess amount of $Fe(NO_3)_3 \cdot 9H_2O$ (0.404 g, 1 mmol) at 600 rpm with reversal of rotation every 30 min over a 24-hour period. Subsequently, the resulting solid was subjected to a washing step with a 0.1 M H_2SO_4 solution to eliminate any unreacted iron salt. The dispersion was then filtered and washed multiple times with distilled water. Finally, the material was dried overnight under vacuum at 120 ºC affording **rGO-dppz@Fe**.

2.2.3. Synthesis of rGO-dppz@Fe(240N$_2$)

The rGO-dppz@Fe material (0.8 g) was thermally treated in a tubular furnace (Carbolite Gero CTF, Parsons Lane, Hope Valley, UK) under a nitrogen atmosphere at 240 °C for 1 hour, using a heating ramp of 10 ºC·min^{-1}. The resulting solid was designated as **rGO-dppz@Fe(240N$_2$)**.

2.3. Instrumental characterization techniques

The total content of carbon, hydrogen and nitrogen present in the samples (CHN analysis) was determined in an elemental microanalyzer Thermo Finnigan Flash EA 1112 series with a Micro TruSpec detection system from LECO. CHN analysis was carried out by dynamic flash combustion of the samples and subsequent detection using a thermal conductivity detector (TCD) after a separation step by Gas Chromatography.

Iron loadings were determined by Inductively Coupled Plasma Mass Spectrometry (ICP-MS) on a PerkinElmer NexION 350X spectrometer equipped with a sample-introducing system, argon plasma ionization and ion detecting quadrupole detection. Prior to the measurement, samples were digested in a Milestone ultraWAVE microwave system.

Raman spectra were acquired in a Renishaw Raman spectrometer (InVia Raman Microscope) provided with a Leica microscope and a coupled charge dispositive detector (CCD). Samples were excited with a 532 nm laser in a Raman shift range of 100-3500 cm^{-1} whilst the signal-to-noise ratio of the spectra was adjusted by optimization of different parameters. Then, a laser power of 10% over the maximum provided, 10 seconds of exposure time and a total of 20 scans per spectrum were stablished.

X-ray diffraction (XRD) patterns were collected using a Bruker D8 discover equipped with a monochromatic Cu-Kα radiation (40 kV and 30 mA, λ = 1.5418 Å) over an angular range of 5 to 80 º and a scan speed of 0.04° per step (1.05 s).

Textural properties of the synthesized solids were evaluated by gas physisorption of nitrogen at liquid nitrogen temperature (−196 °C) using an Autosorb-iQ-2 MP/XR equipment. Prior to analysis, samples were degassed overnight at 120 °C under vacuum. Nitrogen adsorption-desorption isotherms were used to determine pore volumes (V_T), pore sizes (D_{pore}) and surface areas (S_{BET})

Morphological analyses were evaluated by Transmission Electron Microscopy (TEM) and Scanning Electron Microscopy (SEM). TEM images were obtained with a JEOL JEM 1400 microscope operating at 300 kV. Samples were deposited by dropping a sonicated dispersion of the solid in isopropanol over carbon-coated copper grids (Agar Scientific Ltd). Moreover, TEM coupled energy-dispersive X-ray spectroscopy (EDX) was carried out to determine the elemental distribution of the samples in different areas. Alternatively, SEM images were obtained in a JEOL JSM 7800 F microscope.

XPS spectra were collected using SPECS PHOIBOS150MCD X-ray photoelectron spectrometer, operated with a monochromatic Al Kα X-ray source (hv = 1486.7 eV) at 300 W X-ray power, 12 kV of anode voltage and a multichannel detector. Pellets shape

samples were degassed under ultra-high vacuum (Specs™ ultra-high vacuum (UHV) multipurpose surface analysis system) before surface analysis. CasaXPS software was employed for data curation. Charging phenomena were corrected by assigning to the adventitious C1s peak a reference binding energy value of 284.8 eV. XPS spectra deconvolutions were fitted according to Gaussian-Lorentzian functions. Peaks background subtraction was accomplished using a Shirley-type baseline.

2.4. Oxygen evolution reaction (ORR) electrocatalysis

Electrochemical analyses were recorded using a PalmSens4 potentiostat/galvanostat from PalmSens BV in a classical three-electrode cell at room temperature. A glassy carbon disk (GCE, 5 mm in diameter, AFE3T050GC), an Ag/AgCl and a graphite rod electrode were used as working, reference and counter electrodes, respectively. Rotating disk electrochemical (RDE) analysis was performed employing a modulated speed rotator (AFMSRCE model) from Pine Research Company. A 25 μL drop of different samples with a concentration of 5 $mg \cdot mL^{-1}$ was loaded onto the clean surface of the GCE working electrode. In all cases the catalyst loading was 0.125 mg. N_2- or O_2-saturated 0.5 M KOH was used as electrolyte. Nernst equation was used to calibrate potentials according to the reversible hydrogen electrode (RHE), as previously described [75,79]: $E_{RHE} = 0.197\ V + E_{Ag/AgCl} + 0.059 \cdot pH$ (1)

ORR analyses were performed by cyclic voltammetry (CV). The number of electrons transferred per O_2 molecule was calculated by measuring CV curves at different rotation rates from 250 to 2500 rpm and applying Koutecky-Levich (K-L) equations [75,79]:

$$\frac{1}{J} = \frac{1}{J_L} + \frac{1}{J_K} = \frac{1}{B\omega^{1/2}} + \frac{1}{J_K} \quad (2)$$

$$J_K = nFKC_0 \quad (3)$$

$$B = 0.62nFC_0D_0^{2/3}\upsilon^{1/6} = B^*n \quad (4)$$

where J, J_K and J_L are the measured current density, the kinetic and diffusion limiting current densities, respectively; ω is the electrode rotation rate, n is the overall number of electrons transferred during oxygen reduction, F is the Faraday constant, C_0 is the bulk concentration of oxygen dissolved in the electrolyte, D_0 is the oxygen diffusion coefficient, v is the kinematic viscosity of the electrolyte, and k is the electron transfer rate constant during the ORR. B* is a constant ($2.76 \cdot 10^{-5}\ A \cdot cm^{-2} \cdot rpm^{-1/2}$) that is the same for all the performed experiments.

Durability test: To evaluate the stability of rGO-dppz@Fe(240N_2) as an effective ORR electrocatalyst, an accelerated aging test (AAT) was carried out. AAT consisted of performing 1000 CV scans in O_2-saturated 0.5 M KOH solution at scan rate of 0.1 $V \cdot s^{-1}$ in static conditions (i. e. at 0 rpm of rotation rate), and subsequently a RDE curve in the same electrolyte at a scan rate of 0.01 $V \cdot s^{-1}$ and a rotation rate of 2500 rpm.
Methanol resistance test: A chronoamperometric (CA) curve under a constant voltage of 0.45 V (vs. RHE) in O_2-saturated 0.5 M KOH solution for 30 minutes was carried out, being 3M methanol injected after 5 minutes (once CA was started).

2.5. Zinc-air (Zn-air) battery device

A battery cycler BioLogic BCS-810 was used to perform the galvanostatic discharge analysis. rGO-dppz@Fe(240N_2) and 10 wt.% Pt-C (from Sigma Aldrich) were used to prepare the positive electrodes, which were tested in a Zn/KOH-ZnO/air battery. A 45 µL drop of different samples with a concentration of 12.5 $mg \cdot mL^{-1}$ and 5 µL of Nafion solution 5 wt.% (0.563 mg of catalyst) were loaded drop by drop onto a carbon cloth gas diffusion layer (GDL ELAT LT1400W from Fuel Cells Store). A KOH-ZnO (6 M KOH and 0.1 M ZnO) aqueous solution as liquid electrolyte with a final volume of 1 mL, and a Zn plate was used as anode. Nickel meshes were used as current collectors, and the electrode/electrolyte contact areas were always 0.63 cm^2. Galvanostatic discharge curves were carried out at -5 mA.

3. Results and discussion

3.1. Synthesis and characterization of GO-dppz based materials.

Ball-milling synthetic procedure has been considered a sustainable mechanochemical approach to prepare dipyridylpyridazine derived multilayer graphene from Diels-Alder cycloaddition reaction of GP (dienophile) and dptz (diene) [75,78]. The dipyridylpyridazine adducts preferentially located at the edge of the graphene sheets have the ability to serve as ligands for metal coordination similarly to bipyridine-like ligands [77,78,80–82]. Specifically, atomically dispersed edge-enriched FeN_4 active sites can be generated on the graphene-like structure [75]. In this work, **GO** has been firstly obtained from a **graphite** powder by the conventional Hummers method following a previously reported procedure [76]. The next step consisted in the Diels-Alder cycloaddition between **dptz** compound, acting as an electron-deficient diene, and the carbon-carbon double bonds located on the periphery of the GO sheets, acting as dienophiles. Subsequently, the

initial adduct underwent a retro-Diels-Alder reaction, liberating N_2 and leading to the formation of a dihydropyridazine adducts. This surface adducts were further aromatized to yield the corresponding pyridazine by using DDQ as oxidizing agent, affording the sample **rGO-dppz**. The coordination of iron metal centers into dppz adducts through an additional ball-milling process gave rise to **rGO-dppz@Fe**. An additional oxidative cyclodehydrogenation reaction promoted by heating at 240 ºC under nitrogen atmosphere was performed to originate higher proportion of the graphitic-N contributions (quaternary-N) and reduced Fe^{2+} species related to FeN_4 tetracoordinate sites obtaining the resulting material **rGO-dppz@Fe(240N$_2$)** [75,83]. The tentative structures have been proposed in **Figure 1** according to the reactions carried out and the results of characterization (*vide infra*) and the analogy with iron-bipyridine complexes commonly employed for the activation of dioxygen in oxidation reactions of unsaturated hydrocarbons [84,85]. Moreover, the reduction of GO to rGO is predicted to occur due to the mechanochemical processes and the pyrolysis step as previously reported in other studies [86–88].

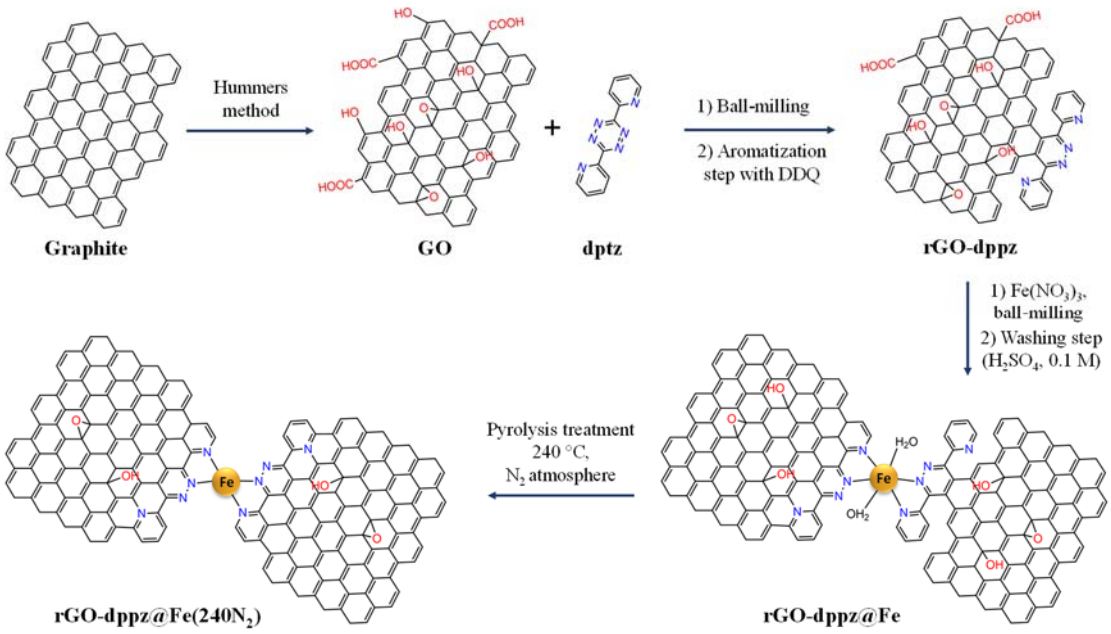

Figure 1. Schematic diagram depicting the synthetic pathway for the preparation of GO-dppz@Fe(240N_2) along with the corresponding proposed structures in each step.

The structural modifications occurred along the synthetic route were examined by XRD and Raman spectroscopy. The XRD patterns of the starting graphite, GO, rGO-dppz, rGO-dppz@Fe and rGO-dppz@Fe(240N_2) are illustrated in **Figure 2A**. XRD spectra of

the starting graphite revealed the characteristic strong peak at ca. 26.5º (2θ) related to the (002) graphite reflection plane and two weak peaks over 44.1º and 54.6º attributed to the (100) and (004) reflections, respectively [89]. Conversely, the (002) diffraction peak was displaced to lower angles up to ca. 12º (2θ) and the lower intensity reflections due to the graphite phase disappeared as a consequence of obtaining GO that increases the interlayer spacing [87]. After the two ball-milling steps for the synthesis of rGO-dppz and rGO-dppz@Fe, the (002) reflection plane underwent some substantial changes. Whilst the reappearance of the diffraction peak at ca. 26.5º (2θ) was observed, the decrease in the intensity of the peak at ca. 12º was noted. These alterations were ascribed to the partial reduction of GO to rGO due to mechanochemical reactions [86]. The pyrolysis process at 240 ºC produced the complete exfoliation and reduction of the GO to rGO and the diffraction patterns of rGO-dppz@Fe(240N_2) exhibited a very broad and low intensity peaks, typical of a graphite-like structure at 2θ=26.5º and 44.1º corresponding to the plane (002) and (100), respectively, while the reflection at ca. 12º attributed to GO based materials was completely absent [76]. The displacement of the peak (002) back to 26.5º resulted from the removal of several oxygenated functional groups, thus decreasing the interlayer spacing [87]. Likewise, the significant broadening of diffraction planes was associated with high disorder in the stacking of reduced graphene sheets [76,88,90]. Moreover, the absence of additional peaks excluded the formation of iron nanoparticles or iron oxides species during the synthetic procedure [63,66].

Further information was obtained from Raman spectroscopy (**Figure 2B**). The starting graphite spectrum exhibits the characteristic D and G bands at 1340 and 1580 cm^{-1}, respectively. The presence of D-peak in graphite-based materials is associated with the breathing modes of sp^2 carbon rings whose intensity varies depending on the C-sp^3 defects, thus indicating the degree of structural disorder [89] which can be promoted by the following aspects: i) defects in the crystalline structure of the graphene sheets, ii) the discontinuities at the boundaries of the graphitic planes, and iii) the modifications occurring on the sp^2 carbon bonds through functionalization reactions [75]. Likewise, G-band is related to the in-plane vibrational modes attributed to the stretching of sp^2 hybridised carbon bonds in both rings and chains [87]. Additionally, the spectrum showed the 2D peak as an overtone of the D peak. The position, the profile of the curve and the intensity of the band enable determine the number of layers in high-quality graphene-based materials [91]. The intensity ratio of the D and G peaks (I_D/I_G) offers a quantitative assessment of the structural irregularity of these materials, uncovering the structural

modifications that have occurred during each stage of synthesis route. The I_D/I_G values increased remarkably from 0.24 for the starting graphite to 0.94 for the GO and 1.01 for the rGO-dppz@Fe(240N_2) due to the increase of the structural disorder and the lower graphitization degree in each material throughout the synthetic process, thus demonstrating the decrease in the average size of the sp^2 domains [76]. The generation of further defects was associated to the chemical treatment for the GO synthesis and subsequent exfoliation and reduction processes produced by the mechanochemical treatments for the obtention of rGO [92]. Therefore, the transformation of graphite to GO and rGO resulted in a notable decrease in the intensity of the 2D and G bands, while significantly enhancing the intensity of the D band [88].

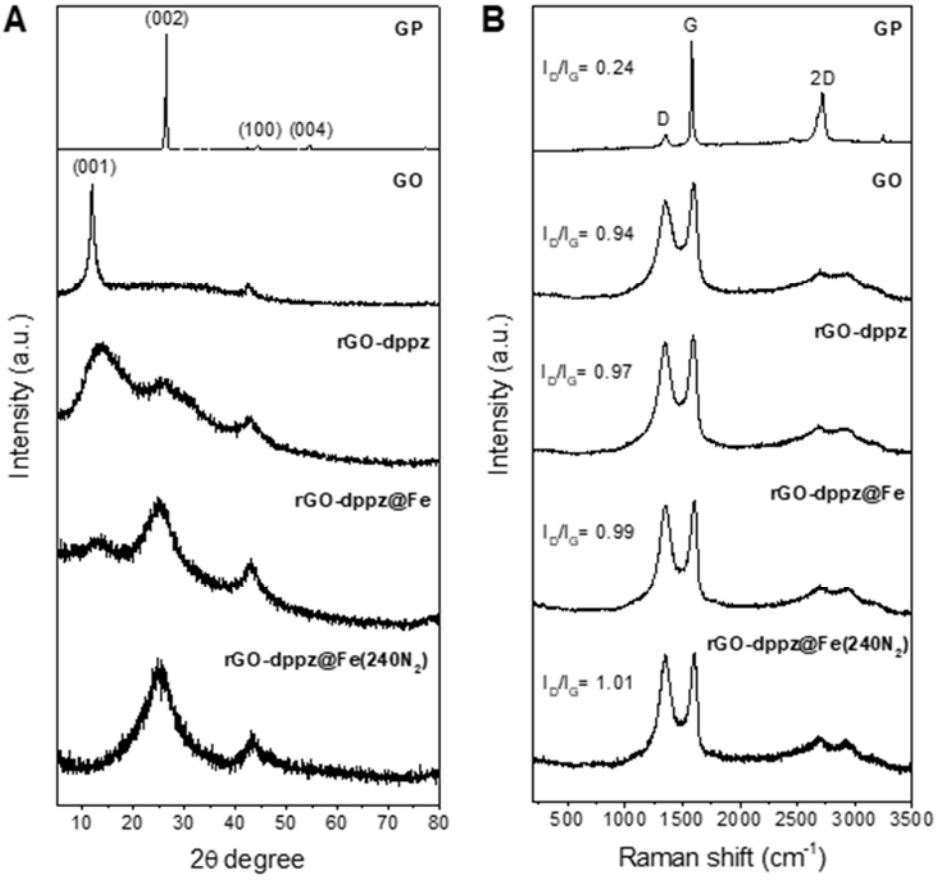

Figure 2. (A) XRD patterns and (B) Raman spectra of the different materials.

Elemental analysis of the four samples (GO, rGO-dppz, rGO-dppz@Fe and rGO-dppz@Fe(240N_2)) provided the C, H and N contents. Conversely, the amount of Fe coordinated on the dppz surface adducts was quantified by ICP-MS (**Table 1**). The percentage of C increased successively from 49.7 % to 69.4 % as a consequence of the

progressive reduction of GO to rGO in each stage. The N content of the rGO-dppz@Fe(240N_2) was 3 wt.% whereas the Fe content was 1 wt.%. Hence, the molar ratio of N/Fe was approximately 12, indicating that in addition to the coordination of one Fe atom to two dipyridylpyridazine units at the edges of distinct graphene sheets to form FeN_4-like sites (**Figure 1**), there were also coordination free dppz surface adducts.

Table 1. Elemental composition of synthesized GO and rGO-dppz materials and N/Fe molar ratio.

Samples	wt.% C	wt.% H	wt.% N	wt.% Fe	N/Fe molar ratio
GO	49.67	3.12	0.02	0.03	-
rGO-dppz	61.02	2.00	4.52	0.04	-
rGO-dppz@Fe	61.30	1.80	2.90	0.77	14.8
rGO-dppz@Fe(240N_2)	69.39	1.25	3.02	0.97	11.9

Textural properties of graphene-based materials were analyzed by N_2 adsorption/desorption isotherms (**Figure 3A**).#A combination of type II and IV isotherms according to the Brunauer-Deming-Deming-Teller (BDDT) classification was obtained for all materials characteristic of macroporous and mesoporous solids, respectively. The acquisition of a mesoporous structure has been demonstrated to be beneficial for the accessibility to large amount of active sites and the enhancement of the mass-transport properties [93]. Brunauer-Emmett-Teller (BET) surface area, pore volume and pore diameter are exposed in **Table 2**. A decrease in the surface area and pore volume was shown as a consequence of the formation of the Diels-Alder surface adduct in the GO sheets, while an increase of pore diameter was produced due to creation of structural defects in the porous structure (**Figure 3B**). Thereafter, the coordination of Fe atoms gave rise to the increase in surface area (ca. 50 $m^2 \cdot g^{-1}$), pore volume (ca. 0.1 $cm^3 \cdot g^{-1}$) and pore diameter (ca. 6.5 nm) attributed to the porous structure generated by the co-formation of rGO material and FeN_4 active sites [75,94,95].

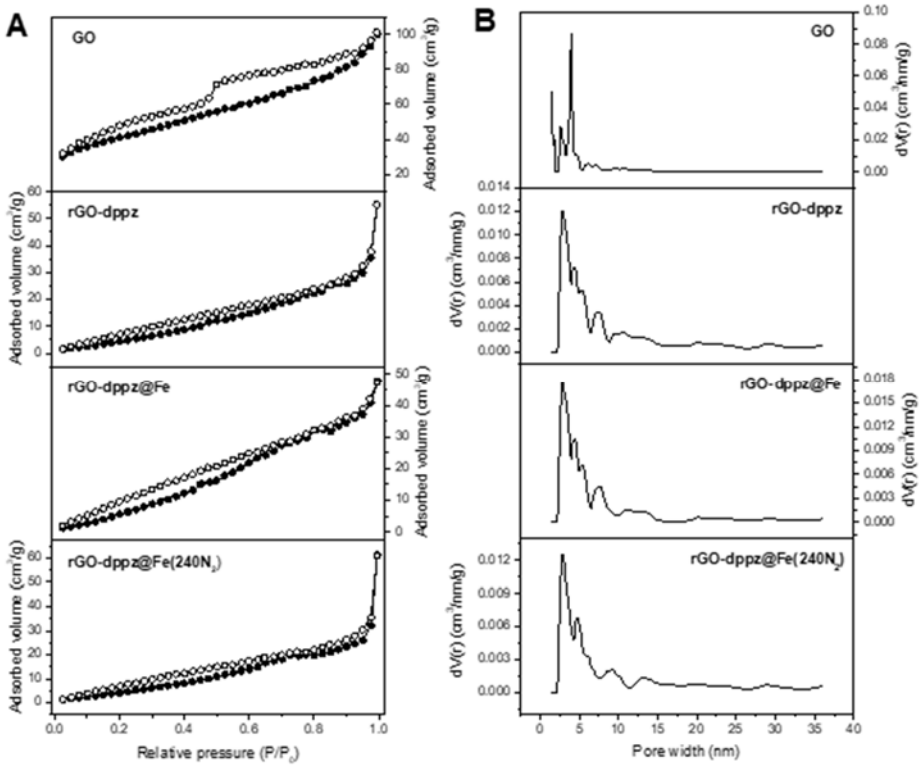

Figure 3. (A) N_2 adsorption/desorption isotherms and (B) pore size distribution of GO and rGO-dppz materials.

Table 2. Textural data of GO and rGO-dppz materials.

Samples	S_{BET} ($m^2 \cdot g^{-1}$)	V_T ($cm^3 \cdot g^{-1}$)	D_{pore} (nm)
GO	145	0.150	2.1
rGO-dppz	32	0.085	5.3
rGO-dppz@Fe	55	0.104	2.7
rGO-dppz@Fe(240N_2)	49	0.095	6.5

The morphology of the rGO-dppz@Fe(240N_2) sample was investigated by SEM and TEM as reported in **Figure 4**. A micrometric and 3D porous network of randomly-oriented wrinkled graphene sheets was evidenced (**Figures 4A** and **4B**) as a consequence of the exfoliation and assembly processes of the GO sheets by the ball-milling steps [76]. TEM micrograph of rGO-dppz@Fe(240N_2) revealed few randomly oriented transparent sheets with wide and flat shapes showing few surface wrinkles (**Figures 4C** and **4D**) [96,97]. The edges of the exfoliated sheets appeared smooth, thus acting as active binding sites for the coordination of Fe atoms between adjacent sheets of rGO.

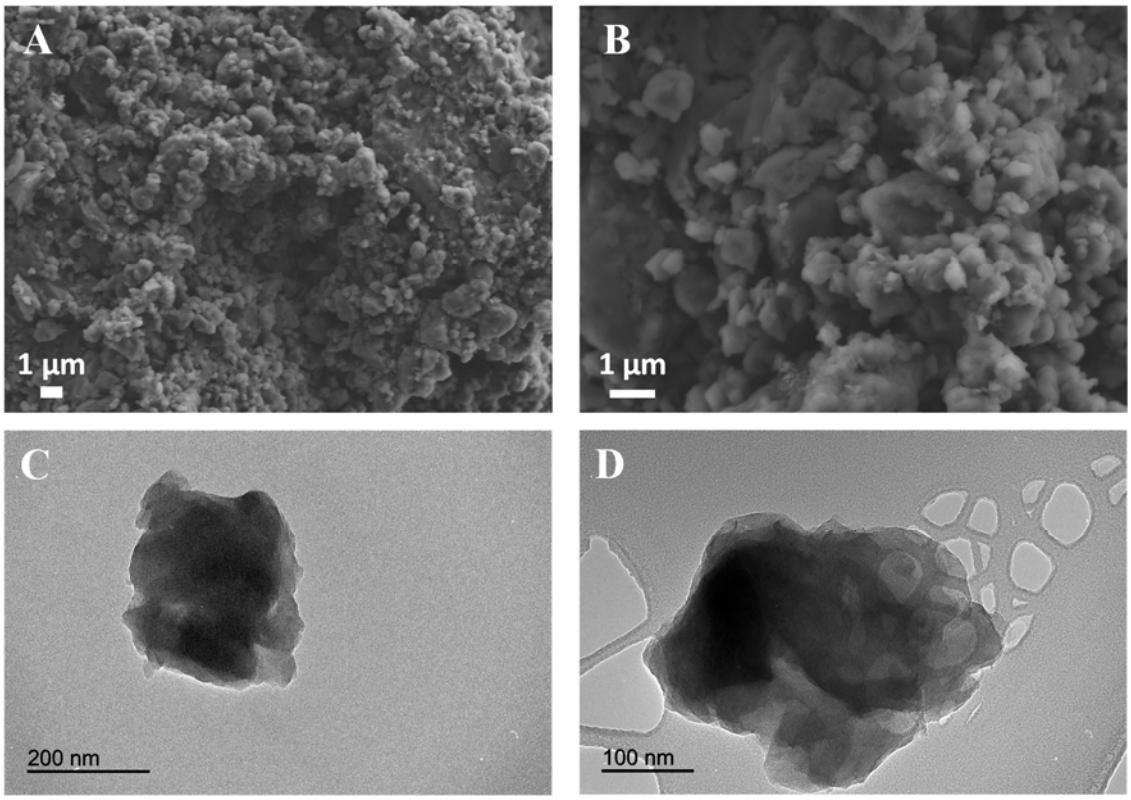

Figure 4. SEM (A, B) and TEM (C, D) representative images of rGO-dppz@Fe(240N_2) at different magnifications.

TEM-EDX mapping was performed to study the elemental distribution throughout rGO-dppz@Fe(240N_2) material. Then, **Figure 5** showed the incorporation of N and Fe atoms homogeneously distributed across the analysed sample without observing colloidal iron oxide particles. Moreover, the overlapping of Fe in N elemental map specially in the central area of the images was evidenced, supporting that the Fe coordination occurred on N atoms of the dppz surface Diels-Alder adducts at the surface and edges of graphene flakes during the post-synthetic metalation reaction with the Fe salt. SEM-EDS images at greater length scale (10 µm) demonstrate the homogeneity of highly dispersed Fe atoms throughout the sample (**Figure S1**), thus corroborating the results obtained in the elemental TEM-EDX mapping for the rGO-dppz@Fe(240N_2) at higher magnification (**Figure 5**).

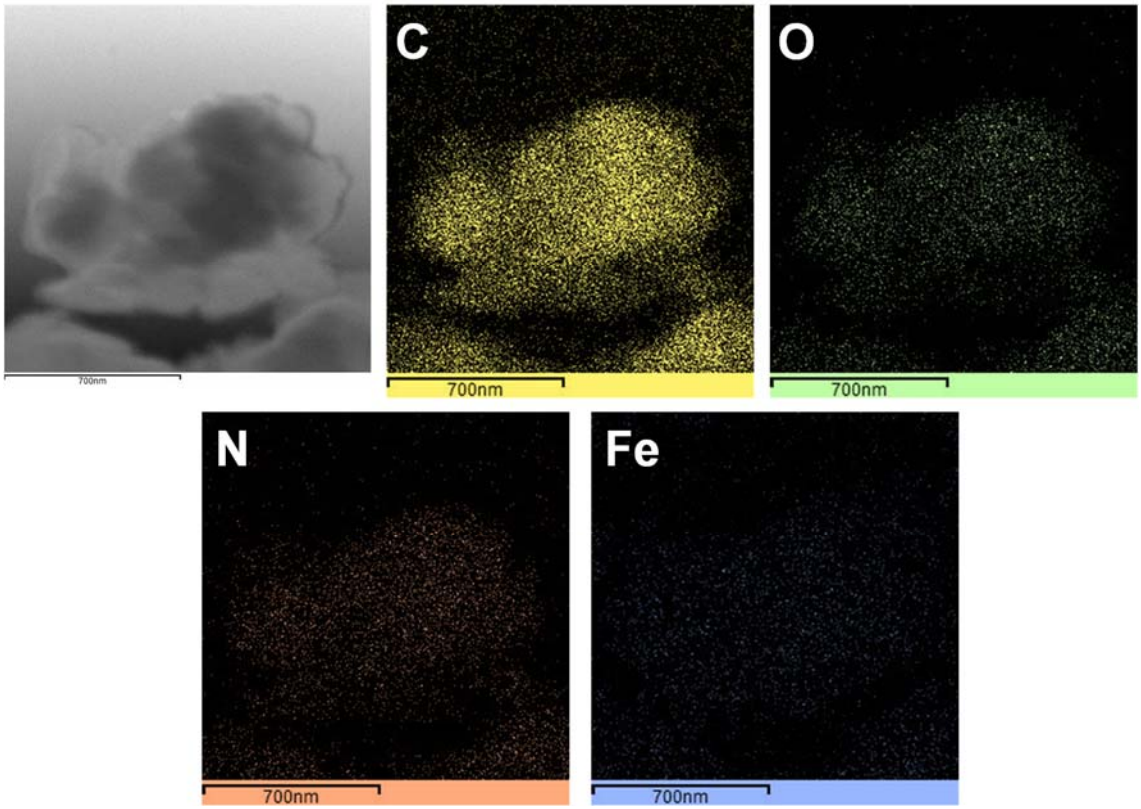

Figure 5. TEM-EDX elemental mapping for the rGO-dppz@Fe(240N_2).

X-ray photoelectron spectroscopy (XPS) was carried out for the study of the surface chemical structure of the materials in each step of the synthesis route (**Figure 6**). C1s high-resolution XPS spectra of the starting GP and GO were deconvoluted into five components associated with C=C/C-C (sp^2/sp^3centers), C-O, C=O, O-C=O and π-π* transitions located at ca. 284.8, 286.7, 288.0, 289.1 and 291.0 eV, respectively (**Figure 6A**). However, the contribution percentages of each curve were significantly different comparing both materials (**Table S1** and **S2**). Whilst GP exhibited the main peak of the C=C/C-C bonds (80.6 %), GO showed an important increase of the carbon-oxygen functional groups, obtaining a contribution of 58.5 % compared with that of 14.4 % calculated for the GP as a result of the oxidation process. After Diels-Alder reaction, a partial reduction of GO to rGO was occurred due to the ball-milling process, experiencing a prominent decrease of the oxygenated carbon contributions (**Figure 6A and Table S3**). Additional components assigned to C-N and C=N bonds from pyridinic, pyridazinic and graphitic-N/quaternary-N species were located at 285.8 and 289.1 eV, respectively. The HR-XPS spectra of N1s (**Figure 6B**) of rGO-dppz material revealed the characteristic contribution of nitrogen belonging to the pyridine and pyridazine rings centered at 399.4 eV. Previous studies have shown that both species produced by Diels-Alder reaction

between graphite-based materials and dipyridyl-tetrazine derivates presented the same signal [78,98]. Moreover, an intense contribution associated to quaternary-N species at 401.4 eV was obtained, possibly as a consequence of the protonation of the N-containing rings by carboxylic acids or from the nucleophilic attack of pyridine molecules on epoxide groups (epoxide ring-opening reactions) [99] of the GO surface forming pyridinium cations. The incorporation of Fe atoms in rGO-dppz material gave rise to a further reduction of GO revealed by the slight decrease in the oxygenated groups with respect to those obtained in the previous stage (**Figure 6A, Table S3**). The N1s signal of rGO-dppz@Fe displayed two new components related to N-oxide groups (403.7 eV) and π-π* transitions (406.1 eV) from aromatic rings and unsaturated bonds [100,101]. An important reduction in the contribution of graphitic-N species was observed due to the breakdown of the ionic interaction between GO and adsorbed dptz units by the successive washing steps with dilute acid aqueous solution (**Figure 6B**). The decrease in N content by ca. 1.6% (**Table 1**) compared to the previous step demonstrated these changes in the chemical structure of rGO-dppz@Fe. However, the formation of quaternary-N was evidenced under the experimental conditions established in this stage of the synthesis route, obtaining a peak contribution of 24.3% (**Table S4**). This behavior, at least in the same extension, was apparently not observed in dppz functionalized multilayer graphene where analogous reaction conditions were used [75]. Therefore, the higher degree of structural disorder and the rich surface chemistry of GO play a key role in the resulting reactivity of these materials, which promoted anticipated oxidative cyclodehydrogenation reactions between bipyridine moieties and graphene sheets [83]. The cyclodehydrogenation processes were even more evident with the heat treatment at 240 ºC under inert atmosphere, which produced an increase in the graphitic-N contribution in rGO-dppz@Fe(240N_2) up to 29.2%, anticipating an improvement of the limiting current density for ORR (**Figure 6B, Table 3**). In addition, the high content of pyridinic-N (56.1%) evidenced the extensive formation of Fe-N bonding along the surface of the rGO sheets [66,102], thus favouring the formation of Fe-N_4 sites, which usually promote improved O_2 transport and so ORR performance. As also demonstrated by the XRD patterns, the further decrease in the relative contributions of the oxygenated groups with respect to the rGO-dppz@Fe material corroborated the essentially complete reduction of GO to rGO in rGO-dppz@Fe(240N_2) (**Figure 6A, Table 3**). No substantial changes in the elemental composition of nitrogen were observed comparing these last two synthesis steps maintaining ca. 3 wt.% N (**Table 1**).

Fe2p XPS spectra of rGO-dppz@Fe and rGO-dppz@Fe(240N_2) materials were deconvoluted into five peaks assigned to Fe^{2+} $2p_{3/2}$, Fe^{3+} $2p_{3/2}$, satellite peak, Fe^{2+} $2p_{1/2}$ and Fe^{3+} $2p_{1/2}$ located at ca. 711.9, 717.2, 720.4, 725.1 and 730.4 eV, respectively [72,103] (**Figure 6C**). The appearance of Fe^{2+} 2p signals confirmed the formation of the FeN_4 sites after the ball milling process. However, the contribution of the reduced Fe^{2+} species was clearly increased as a consequence of the heat treatment at 240 ºC, in agreement with previous studies [75,104–106]. In fact, the Fe^{2+}/Fe^{3+} ratio was raised from 2.11 to 3.46 for rGO-dppz@Fe and rGO-dppz@Fe(240N_2), respectively.

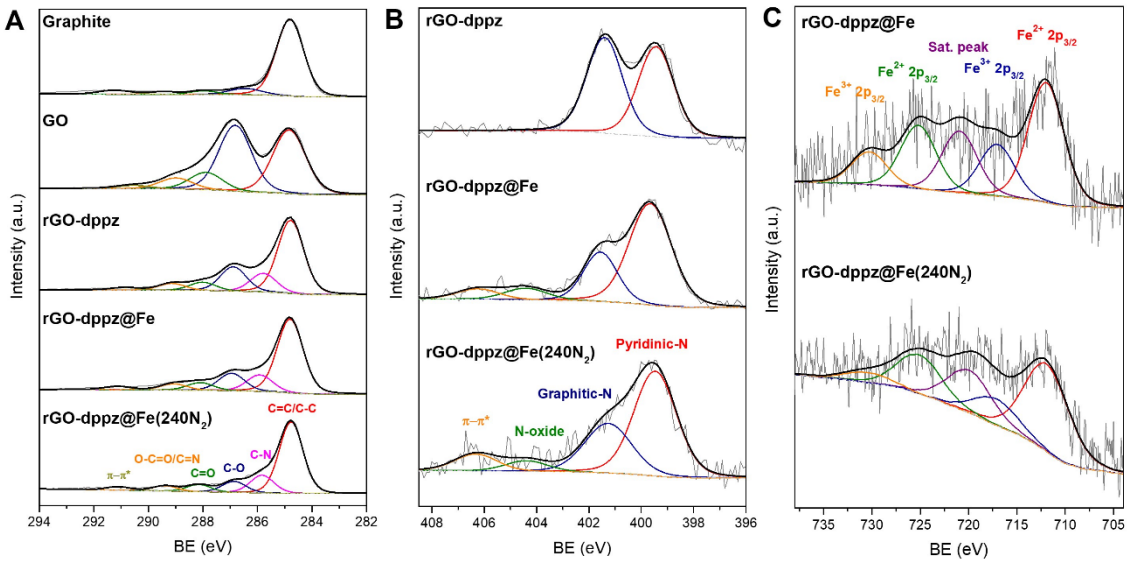

Figure 6. (A) C1s, (B) N1s and (C) Fe2p HR-XPS spectra of materials.

Table 3. Contribution of the components used in the fitting of the C1s, N1s and Fe2p photoemission peaks for rGO-dppz@Fe(240N_2).

	Surface groups	BE (eV)	Atom %
C1s	C=C/C-C	284.8	61.4
	C-N	285.8	15.2
	C-O	286.9	9.6
	C=O	288.1	6.2
	O-C=O/C=N	289.4	4.6
	π-π*	291.1	3.0
N1s	Pyridinic-N	399.5	56.1
	Graphitic-N	401.5	29.2
	N-oxide	404.7	5.7

	π-π*	406.5	9.0
Fe2p	Fe^{2+}	711.9, 725.1	61.5
	Fe^{3+}	717.2, 730.4	17.8

3.2. Electrocatalytic activity of GO and rGO-dppz based materials toward ORR

After characterization, the ORR electrocatalytic properties of the rGO-dppz@Fe(240N_2), rGO-dppz@Fe, rGO-dppz and bare GO were evaluated by cyclic voltametric (CV) in a traditional three-electrode cell, as detailed in experimental section. **Figure 7A** shows the resulting CV curves under N_2-saturated atmosphere, whilst **Figure 7B** displays the same curves under O_2-saturated conditions, confirming that cathodic peaks correspond to oxygen electroreduction. In addition, **Figure 7B** shows the different ORR performance for the different samples. Onset values of 0.83, 0.80, 0.79, 0.77 and 0.85 V vs RHE, and maximum current densities of -0.88, -0.85, -0.57, -0.46 and -0.56 $mA \cdot cm^{-2}$ were obtained for rGO-dppz@Fe(240N_2), rGO-dppz@Fe, rGO-dppz, bare GO and 10 % wt Pt-C, respectively, demonstrating the superior catalytic properties of rGO-dppz@Fe(240N_2). These results clearly evidenced that the synthesis process favored the incorporation of FeN_4 sites into the rGO structures. Moreover, it should be noted that onset and current density values (0.80 V vs RHE and -0.88 $mA \cdot cm^{-2}$) obtained for rGO-dppz@Fe(240N_2) improve significatively those reported with a multilayer graphitic structure functionalized with dppz Diels-Alder adducts coordinating FeN_4 sites, that provided an onset potential of 0.82 V vs. RHE and maximum current density of -0.83 $mA \cdot cm^{-2}$ [75].

Next, the analysis of ORR kinetics for the different samples and 10 wt.% Pt-C as reference were carried out using rotating-disk voltammograms (RDVs), which were acquired at several rotation rates in O_2 saturated 0.5 M KOH aqueous solution. **Figure S2** shows the resulting RDV curves for the different samples at all rotation rates. In all cases, an increase of the limited current densities can be observed with the rotation rate increase, which is typical of a diffusion-controlled electrochemical process [79]. **Figure 7C** compares the resulting RDV curve at the same rotation rate of 2500 rpm for all samples, including 10 wt.% Pt-C as a reference material. Overall, rGO-dppz@Fe(240N_2) provided better features, in terms of both onset potential (**Table 4**) and limited current density (J_K) than those obtained for rGO-dppz@Fe, rGO-dppz and bare GO. And against the reference material, rGO-dppz@Fe(240N_2) provided better limited current density but slightly worse onset potential than 10 wt.% Pt-C. RDV curves were also recorded at 1600 rpm, as shown in **Figure S3**, to calculate the half-wave potentials, which were included in

Table 4. **Figure 7D** shows the resulting Koutecky-Levich (K-L) plots for the different samples. The excellent linear fitting indicates a first-order reaction kinetics. In addition, K-L plots were used to calculate different kinetics parameters such as transferred electrons (n) per oxygen molecule and J_K (**Table 4**). In summary, the studies performed under static and dynamic conditions confirmed that rGO-dppz@Fe(240N_2) provides the best ORR electrocatalytic performance under alkaline conditions, demonstrating that the proposed modification of the starting GO improved significatively its catalytic properties. In the durability test (**Figure 7E**), an improvement in the onset potential and a slight decrease in the maximum current density, demonstrating the excellent stability of the rGO-dppz@Fe(240N_2) electrocatalyst can be observed. This improvement in the onset potential could be attributed to a complete reduction of any GO, which was partially reduced to rGO, whilst the slight decrease in current density would be associated with the loss of material deposited on the GCE surface after the AAT. **Figure 7F** shows that rGO-dppz@Fe(240N_2) exhibits better resistibility to methanol than 10 % wt Pt-C.

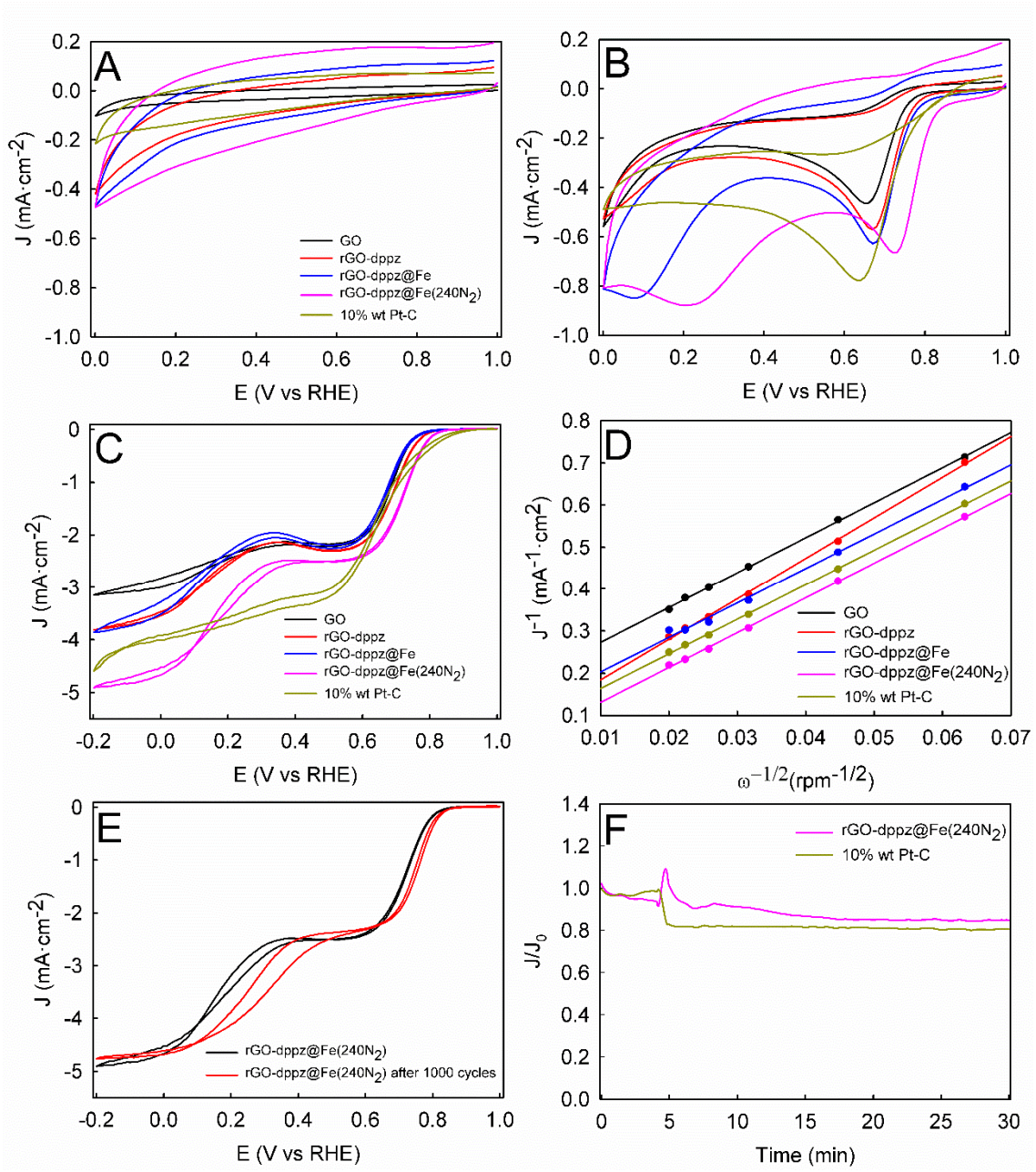

Figure 7. CV curves obtained for the different samples in N_2-satured (A) and O_2-satured (B) in 0.5 M KOH at 0.1 $V \cdot s^{-1}$. (C) RDV curves of all samples at the same rotating rate of 2500 rpm and a scan rate of 10 $mV \cdot s^{-1}$. (D) K-L plots obtained from the RDVs in **Figure S2** at 0.0 V vs RHE. (E) RDE curves of rGO-dppz@Fe(240N_2) before and after 1000 cycles of the AAT, in O_2-saturated 0.5 M KOH at rotating rate of 2500 rpm and with scan rate of 0.01 $V \cdot s^{-1}$. (F) Chronoamperometric curves of rGO-dppz@Fe(240N_2) and 10 % wt Pt-C after injection of 3 M methanol.

Table 4. ORR Kinetics parameters obtained from the RDVs in **Figure S2** at 0.0 V vs RHE.

Parameter	GO	rGO-dppz	rGO-dppz@Fe	rGO-dppz@Fe(240N_2)	10 wt.% Pt-C
E_{onset} (V)	0.74	0.78	0.75	0.80	0.85
$E_{half\text{-}wave}$ (V)	0.70	0.71	0.70	0.75	-
n	4.35	3.76	4.37	4.41	4.39
J_k (mA·cm^{-2})	52.64	113.72	82.76	209.33	123.01

3.3. Zn–air battery performance of rGO-dppz@Fe(240N_2) ORR electrocatalyst

Furthermore, to validate the excellent cathodic features of rGO-dppz@Fe(240N_2) for O_2 transport ORR, a ZAB was built to investigate their possible application in a real device. During operation, the attainment of high power density in zinc-air batteries relies on the establishment of adequate three-phase boundaries involving the electrolyte, ORR catalysts, and oxygen [66]. Hence, the oxygen supply from air electrode was crucial to enable the formation of abundant liquid/solid/gas interfaces essential for efficient power generation. rGO-dppz@Fe(240N_2) and 10 wt.% Pt-C were tested as positive electrode, using the same amount of catalyst (0.563 mg), Zn plate as anode and KOH-ZnO (6 M and 0.1 M, respectively) as liquid electrolyte. **Figure 8A** shows the galvanostatic discharge for rGO-dppz@Fe(240N_2) at different intensities (firstly from 1 mA to 20 mA, and later from 20 mA to 1 mA) confirming the remarkable behaviour of this material as cathode in Zn-air batteries. The potential values obtained demonstrated not only the stability of rGO-dppz@Fe(240N_2) but also the excellent battery performance recovery.

Subsequently, a comparative study of the maximum discharge capacity at -5 mA for rGO-dppz@Fe(240N_2) and 10 wt.% Pt-C as air electrodes was carried out (**Figure 8B**). rGO-dppz@Fe(240N_2) presented a higher voltage and a lower potential loss than 10 wt.% Pt-C. In addition, the maximum discharge capacity values were reached for rGO-dppz@Fe(240N_2), which were greater than those obtained with 10 wt.% Pt-C both at -1 and -5 mA (**Table 5**). This result significantly enhanced the specific capacities reported previously for others graphene-Fe based catalysts, demonstrating the outstanding efficiency of rGO-dppz@Fe(240N_2) as cathode in primary ZABs (**Table S1**) [107]. It should be noted that these specific capacities were calculated using the exact weight of active material loaded on the cathode plus the weight of the used GDL (carbon paper). We consider that it was a more appropriate method to calculate the specific capacity of the ZAB than those based on the mass of Zinc consumed, mainly due to the formation of of ZnO or $Zn(OH)_2$ on the surface of the Zinc foil during the discharge process (**Figure S4**).

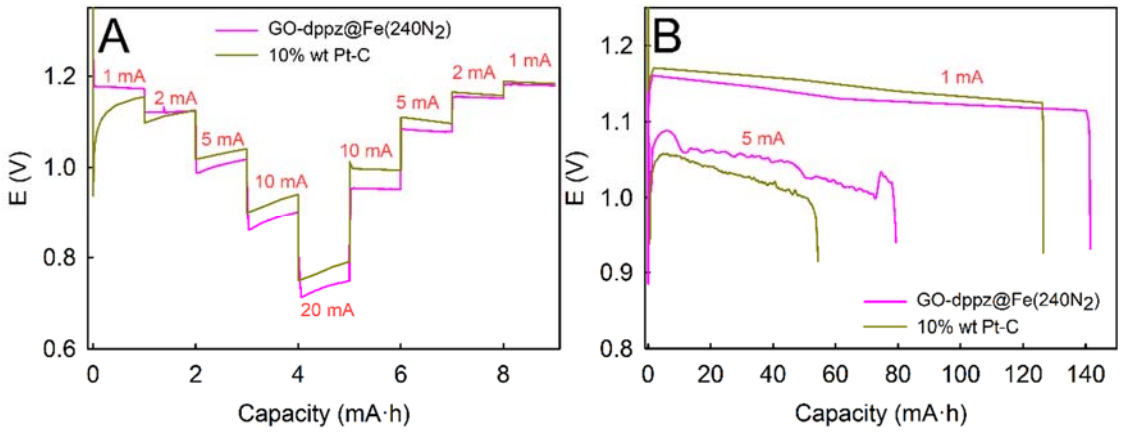

Figure 8. (A) Galvanostatic discharge curves of rGO-dppz@Fe(240N_2) and 10 wt.% Pt-C at different intensities. (B) Galvanostatic discharge curves of rGO-dppz@Fe(240N_2) and 10 wt.% Pt-C at -1 and -5 mA, respectively.

Table 5. Specific capacity values obtained for ZAB based on GO-dppz@Fe(240N_2) and 10% wt Pt-C.

Catalyst	**Specific Capacities ($A \cdot h \cdot g^{-1}$)**	
	-1 mA	**-5 mA**
GO-dppz@Fe(240N_2)	4.94	2.77
10% wt Pt-C	4.41	1.89

4. Conclusions

A solvent-free mechanochemical synthesis route and a thermal treatment at mild temperature were carried out for the preparation of dppz functionalized reduced graphene oxide bearing coordinated FeN_4 active sites through chelating bipyridine units. The characterization results revealed a successive reduction of the starting GO to rGO at each stage of the synthesis process. In addition, graphitic-N species were produced during the Diels-Alder reaction and the subsequent reaction with the iron salt suggesting that: i) pyridinium cations were generated through an acid-base equilibrium with acid-oxygenated functional groups, ii) epoxide ring -opening reactions were produced by the nucleophilic attack of the pyridine molecules and iii) oxidative cyclodehydrogenation

reactions between the dppz units and the rGO sheets occurred spontaneously as a consequence of the high temperatures and pressures reached in the shocks produced during the ball-milling processes. Clearly, the mild thermal treatment promoted an increase in these cyclodehydrogenation reactions, enhancing the graphitic-N contribution. Likewise, this last stage at 240 ºC led to a further reduction of Fe^{3+} species to Fe^{2+}, achieving a Fe^{2+}/Fe^{3+} ratio of ca. 3.5 and a total iron atomic percentage of ca. 1.0 wt.%. Therefore, the high amount of Fe^{2+} and pyridinic-N led to the formation of high-density of catalytically FeN_4 active sites for ORR electrocatalysis. rGO-dppz@Fe(240N_2) material provided better electrocatalytic activity in terms of limited current density than those obtained for rGO-dppz@Fe, rGO-dppz, bare GO and even reference electrode 10 wt.% Pt-C. A flooded ZAB-based on rGO-dppz@Fe(240N_2) ORR electrocatalyst as cathodic material was also built. It exhibited an outstanding specific capacity of 141.1 $A \cdot h \cdot g^{-1}$, which improved the catalytic performance obtained for the 10 wt.% Pt-C benchmark electrocatalyst.

Acknowledgements

The authors wish to acknowledge the financial support from Andalusian Regional Government (Project ProyExcel_00492 and FQM-346 group), Feder Funds, Spanish Ministry of Science and Innovation for a FPU (FPU17/03981) and a FPI (PRE2019-089122) teaching and research fellowships and the projects RTI2018-101611-B-I00 and PDC2022-133973-I00, and the technical staff from the Instituto Químico para la Energía y el Medioambiente (IQUEMA) and Servicios Centrales de Apoyo a la Investigación (SCAI) de la Universidad de Córdoba. A. Benítez is supported by a "Juan de la Cierva – Incorporación" fellowship (IJC2020-045041-I), funded by MCIN/AEI/10.13039/501100011033 and the European Union "NextGenerationEU/PRTR". J. J. Giner-Casares and A. J. Fernandez-Romero also acknowledge the financial support by Spanish Ministry of Science and Innovation through the PID2020-112744GB-I00/AEI/10.13039/501100011033 and PID2019-104272RB-C55/AEI/10.13039/501100011033 plus TED2021-130334B-I00 projects, respectively.

5. References

[1] M.A. Hajer, P. Pelzer, 2050—An Energetic Odyssey: Understanding 'Techniques of Futuring' in the transition towards renewable energy, Energy Res. Soc. Sci. 44

(2018) 222–231. doi:10.1016/j.erss.2018.01.013.

[2] A. García-Olivares, J. Solé, O. Osychenko, Transportation in a 100% renewable energy system, Energy Convers. Manag. 158 (2018) 266–285. doi:10.1016/j.enconman.2017.12.053.

[3] U. Bhattarai, T. Maraseni, A. Apan, Assay of renewable energy transition: A systematic literature review, Sci. Total Environ. 833 (2022) 155159. doi:10.1016/j.scitotenv.2022.155159.

[4] S. Pinteus, P. Susano, C. Alves, J. Silva, A. Martins, R. Pedrosa, Seaweed's Role in Energetic Transition—From Environmental Pollution Challenges to Enhanced Electrochemical Devices, Biology (Basel). 11 (2022) 458. doi:10.3390/biology11030458.

[5] S. Ould Amrouche, D. Rekioua, T. Rekioua, S. Bacha, Overview of energy storage in renewable energy systems, Int. J. Hydrogen Energy. 41 (2016) 20914–20927. doi:10.1016/J.IJHYDENE.2016.06.243.

[6] Y. Yang, S. Bremner, C. Menictas, M. Kay, Battery energy storage system size determination in renewable energy systems: A review, Renew. Sustain. Energy Rev. 91 (2018) 109–125. doi:10.1016/j.rser.2018.03.047.

[7] S. Maddukuri, D. Malka, M.S. Chae, Y. Elias, S. Luski, D. Aurbach, On the challenge of large energy storage by electrochemical devices, Electrochim. Acta. 354 (2020) 136771. doi:10.1016/j.electacta.2020.136771.

[8] Q. Abbas, M. Mirzaeian, M.R.C. Hunt, P. Hall, R. Raza, Current State and Future Prospects for Electrochemical Energy Storage and Conversion Systems, Energies. 13 (2020) 5847. doi:10.3390/en13215847.

[9] N. Ding, K. Prasad, T.T. Lie, The electric vehicle: a review, Int. J. Electr. Hybrid Veh. 9 (2017) 49. doi:10.1504/IJEHV.2017.082816.

[10] X. Sun, Z. Li, X. Wang, C. Li, Technology Development of Electric Vehicles: A Review, Energies. 13 (2019) 90. doi:10.3390/en13010090.

[11] I. Husain, B. Ozpineci, M.S. Islam, E. Gurpinar, G.J. Su, W. Yu, S. Chowdhury, L. Xue, D. Rahman, R. Sahu, Electric Drive Technology Trends, Challenges, and Opportunities for Future Electric Vehicles, Proc. IEEE. 109 (2021) 1039–1059. doi:10.1109/JPROC.2020.3046112.

[12] S.O. Ganiyu, C.A. Martínez-Huitle, The use of renewable energies driving electrochemical technologies for environmental applications, Curr. Opin. Electrochem. 22 (2020) 211–220. doi:10.1016/j.coelec.2020.07.007.

[13] A.A. Kebede, T. Kalogiannis, J. Van Mierlo, M. Berecibar, A comprehensive review of stationary energy storage devices for large scale renewable energy sources grid integration, Renew. Sustain. Energy Rev. 159 (2022) 112213. doi:10.1016/j.rser.2022.112213.

[14] Z.P. Cano, D. Banham, S. Ye, A. Hintennach, J. Lu, M. Fowler, Z. Chen, Batteries and fuel cells for emerging electric vehicle markets, Nat. Energy. 3 (2018) 279–289. doi:10.1038/s41560-018-0108-1.

[15] H.-F. Wang, Q. Xu, Materials Design for Rechargeable Metal-Air Batteries, Matter. 1 (2019) 565–595. doi:10.1016/j.matt.2019.05.008.

[16] Y. Wang, D.F. Ruiz Diaz, K.S. Chen, Z. Wang, X.C. Adroher, Materials, technological status, and fundamentals of PEM fuel cells – A review, Mater. Today. 32 (2020) 178–203. doi:10.1016/j.mattod.2019.06.005.

[17] S. Zaman, L. Huang, A.I. Douka, H. Yang, B. You, B.Y. Xia, Oxygen Reduction Electrocatalysts toward Practical Fuel Cells: Progress and Perspectives, Angew. Chem. Int. Ed. 133 (2021) 17976–17996. doi:10.1002/ange.202016977.

[18] A.G. Olabi, E.T. Sayed, T. Wilberforce, A. Jamal, A.H. Alami, K. Elsaid, S.M.A. Rahman, S.K. Shah, M.A. Abdelkareem, Metal-Air Batteries—A Review, Energies. 14 (2021) 7373. doi:10.3390/en14217373.

[19] M.M. Tellez-Cruz, J. Escorihuela, O. Solorza-Feria, V. Compañ, Proton Exchange Membrane Fuel Cells (PEMFCs): Advances and Challenges, Polymers (Basel). 13 (2021) 3064. doi:10.3390/polym13183064.

[20] D.D.T. Ferraren-De Cagalitan, M.L.S. Abundo, A review of biohydrogen production technology for application towards hydrogen fuel cells, Renew. Sustain. Energy Rev. 151 (2021) 111413. doi:10.1016/j.rser.2021.111413.

[21] Z. Xia, X. Zhang, H. Sun, S. Wang, G. Sun, Recent advances in multi-scale design and construction of materials for direct methanol fuel cells, Nano Energy. 65 (2019) 104048. doi:10.1016/j.nanoen.2019.104048.

[22] R.R. Contreras, J. Almarza, L. Rincón, Molten carbonate fuel cells: a technological perspective and review, Energy Sources, Part A Recover. Util. Environ. Eff. (2021) 1–15. doi:10.1080/15567036.2021.2013346.

[23] M. Singh, D. Zappa, E. Comini, Solid oxide fuel cell: Decade of progress, future perspectives and challenges, Int. J. Hydrogen Energy. 46 (2021) 27643–27674. doi:10.1016/j.ijhydene.2021.06.020.

[24] J. Zhang, Q. Zhou, Y. Tang, L. Zhang, Y. Li, Zinc–air batteries: are they ready

for prime time?, Chem. Sci. 10 (2019) 8924–8929. doi:10.1039/C9SC04221K.

[25] P. Goel, D. Dobhal, R.C. Sharma, Aluminum–air batteries: A viability review, J. Energy Storage. 28 (2020) 101287. doi:10.1016/J.EST.2020.101287.

[26] W.K. Tan, G. Kawamura, H. Muto, A. Matsuda, Current progress in the development of Fe-air batteries and their prospects for next-generation batteries, in: Sustain. Mater. Next Gener. Energy Devices, Elsevier, 2021: pp. 59–83. doi:10.1016/B978-0-12-820628-7.00003-4.

[27] Z. Wu, Y. Tian, H. Chen, L. Wang, S. Qian, T. Wu, S. Zhang, J. Lu, Evolving aprotic Li–air batteries, Chem. Soc. Rev. 51 (2022) 8045–8101. doi:10.1039/D2CS00003B.

[28] C. Pozo-Gonzalo, N. Ortiz-Vitoriano, Recent progress, advances, and future prospects in Na–O2 batteries, Curr. Opin. Electrochem. 36 (2022) 101120. doi:10.1016/j.coelec.2022.101120.

[29] W. Fang, J. Zhao, W. Zhang, P. Chen, Z. Bai, M. Wu, Recent progress and future perspectives of flexible Zn-Air batteries, J. Alloys Compd. 869 (2021) 158918. doi:10.1016/j.jallcom.2021.158918.

[30] Y. Zhang, Y.-P. Deng, J. Wang, Y. Jiang, G. Cui, L. Shui, A. Yu, X. Wang, Z. Chen, Recent Progress on Flexible Zn-Air Batteries, Energy Storage Mater. 35 (2021) 538–549. doi:10.1016/j.ensm.2020.09.008.

[31] K.W. Leong, Y. Wang, M. Ni, W. Pan, S. Luo, D.Y.C. Leung, Rechargeable Zn-air batteries: Recent trends and future perspectives, Renew. Sustain. Energy Rev. 154 (2022) 111771. doi:10.1016/J.RSER.2021.111771.

[32] N.-Q. Meng, Y.-X. Fan, J.-S. Cai, Zn–air batteries for electric vehicles, Tungsten. 1 (2022) 1–10. doi:10.1007/s42864-022-00149-2.

[33] A. Iqbal, O.M. El-Kadri, N.M. Hamdan, Insights into rechargeable Zn-air batteries for future advancements in energy storing technology, J. Energy Storage. 62 (2023) 106926. doi:10.1016/j.est.2023.106926.

[34] N. Shang, K. Wang, M. Wei, Y. Zuo, P. Zhang, H. Wang, Z. Chen, P. Pei, Challenges for large scale applications of rechargeable Zn–air batteries, J. Mater. Chem. A. 10 (2022) 16369–16389. doi:10.1039/D2TA04294K.

[35] S. Ren, X. Duan, S. Liang, M. Zhang, H. Zheng, Bifunctional electrocatalysts for Zn–air batteries: recent developments and future perspectives, J. Mater. Chem. A. 8 (2020) 6144–6182. doi:10.1039/C9TA14231B.

[36] P. Chen, K. Zhang, D. Tang, W. Liu, F. Meng, Q. Huang, J. Liu, Recent Progress

in Electrolytes for Zn–Air Batteries, Front. Chem. 8 (2020) 372. doi:10.3389/fchem.2020.00372.

[37] T. Zhou, N. Zhang, C. Wu, Y. Xie, Surface/interface nanoengineering for rechargeable Zn–air batteries, Energy Environ. Sci. 13 (2020) 1132–1153. doi:10.1039/C9EE03634B.

[38] X. Liu, G. Zhang, L. Wang, H. Fu, Structural Design Strategy and Active Site Regulation of High-Efficient Bifunctional Oxygen Reaction Electrocatalysts for Zn–Air Battery, Small. 17 (2021) 2006766. doi:10.1002/smll.202006766.

[39] O. Ola, N. Wang, G. Walker, Y. Zhu, D. Grant, Engineering the next generation of photorechargeable zinc-air batteries, Curr. Opin. Electrochem. 35 (2022) 101040. doi:10.1016/j.coelec.2022.101040.

[40] H. Liu, W. Xie, Z. Huang, C. Yao, Y. Han, W. Huang, Recent Advances in Flexible Zn–Air Batteries: Materials for Electrodes and Electrolytes, Small Methods. 6 (2022) 2101116. doi:10.1002/smtd.202101116.

[41] V. Caramia, B. Bozzini, Materials science aspects of zinc–air batteries: a review, Mater. Renew. Sustain. Energy. 3 (2014) 28. doi:10.1007/s40243-014-0028-3.

[42] X. Cai, L. Lai, J. Lin, Z. Shen, Recent advances in air electrodes for Zn–air batteries: electrocatalysis and structural design, Mater. Horizons. 4 (2017) 945–976. doi:10.1039/C7MH00358G.

[43] X. Chen, Z. Zhou, H.E. Karahan, Q. Shao, L. Wei, Y. Chen, Recent Advances in Materials and Design of Electrochemically Rechargeable Zinc–Air Batteries, Small. 14 (2018) 1801929. doi:10.1002/smll.201801929.

[44] X. Zhang, L. Wang, H. Fu, Recent advances in rechargeable Zn-based batteries, J. Power Sources. 493 (2021) 229677. doi:10.1016/j.jpowsour.2021.229677.

[45] M. Luo, W. Sun, B. Bin Xu, H. Pan, Y. Jiang, Interface Engineering of Air Electrocatalysts for Rechargeable Zinc–Air Batteries, Adv. Energy Mater. 11 (2021) 2002762. doi:10.1002/aenm.202002762.

[46] H. Liu, Q. Liu, Y. Wang, Y. Wang, S. Chou, Z. Hu, Z. Zhang, Bifunctional carbon-based cathode catalysts for zinc-air battery: A review, Chinese Chem. Lett. 33 (2022) 683–692. doi:10.1016/j.cclet.2021.07.038.

[47] Y. Huang, Y. Wang, C. Tang, J. Wang, Q. Zhang, Y. Wang, J. Zhang, Atomic Modulation and Structure Design of Carbons for Bifunctional Electrocatalysis in Metal–Air Batteries, Adv. Mater. 31 (2019) 1803800. doi:10.1002/adma.201803800.

[48] L. Zong, X. Chen, S. Dou, K. Fan, Z. Wang, W. Zhang, Y. Du, J. Xu, X. Jia, Q. Zhang, X. Li, Y. Deng, Y. Chen, L. Wang, Stable confinement of Fe/Fe3C in Fe, N-codoped carbon nanotube towards robust zinc-air batteries, Chinese Chem. Lett. 32 (2021) 1121–1126. doi:10.1016/j.cclet.2020.08.029.

[49] R. Cao, J.-S. Lee, M. Liu, J. Cho, Recent Progress in Non-Precious Catalysts for Metal-Air Batteries, Adv. Energy Mater. 2 (2012) 816–829. doi:10.1002/aenm.201200013.

[50] S. Wang, H. Jiang, L. Song, Recent Progress in Defective Carbon-Based Oxygen Electrode Materials for Rechargeable Zink-Air Batteries, Batter. Supercaps. 2 (2019) 509–523. doi:10.1002/batt.201900001.

[51] D. Yang, D. Chen, Y. Jiang, E.H. Ang, Y. Feng, X. Rui, Y. Yu, Carbon-based materials for all-solid-state zinc–air batteries, Carbon Energy. 3 (2021) 50–65. doi:10.1002/cey2.88.

[52] J. Zhao, D. Wei, C. Zhang, Q. Shao, V. Murugadoss, Z. Guo, Q. Jiang, X. Yang, An Overview of Oxygen Reduction Electrocatalysts for Rechargeable Zinc-Air Batteries Enabled by Carbon and Carbon Composites, Eng. Sci. 15 (2021) 1–19. doi:10.30919/es8d420.

[53] Q. Zhang, J. Guan, Applications of Atomically Dispersed Oxygen Reduction Catalysts in Fuel Cells and Zinc–Air Batteries, Energy Environ. Mater. 4 (2021) 307–335. doi:10.1002/eem2.12128.

[54] W. Shao, R. Yan, M. Zhou, L. Ma, C. Roth, T. Ma, S. Cao, C. Cheng, B. Yin, S. Li, Carbon-Based Electrodes for Advanced Zinc-Air Batteries: Oxygen-Catalytic Site Regulation and Nanostructure Design, Electrochem. Energy Rev. 6 (2023) 11. doi:10.1007/s41918-023-00181-x.

[55] T. Van Khai, H.G. Na, D.S. Kwak, Y.J. Kwon, H. Ham, K.B. Shim, H.W. Kim, Significant enhancement of blue emission and electrical conductivity of N-doped graphene, J. Mater. Chem. 22 (2012) 17992. doi:10.1039/c2jm33194b.

[56] Y. Zhang, J. Ge, L. Wang, D. Wang, F. Ding, X. Tao, W. Chen, Manageable N-doped Graphene for High Performance Oxygen Reduction Reaction, Sci. Rep. 3 (2013) 2771. doi:10.1038/srep02771.

[57] Y. Lin, K. Liu, K. Chen, Y. Xu, H. Li, J. Hu, Y.-R. Lu, T.-S. Chan, X. Qiu, J. Fu, M. Liu, Tuning Charge Distribution of FeN 4 via External N for Enhanced Oxygen Reduction Reaction, ACS Catal. 11 (2021) 6304–6315. doi:10.1021/acscatal.0c04966.

[58] Y. Zhan, J. Huang, Z. Lin, X. Yu, D. Zeng, X. Zhang, F. Xie, W. Zhang, J. Chen, H. Meng, Iodine/nitrogen co-doped graphene as metal free catalyst for oxygen reduction reaction, Carbon N. Y. 95 (2015) 930–939. doi:10.1016/j.carbon.2015.09.024.

[59] J. Zhang, J. Wang, Z. Wu, S. Wang, Y. Wu, X. Liu, Heteroatom (Nitrogen/Sulfur)-Doped Graphene as an Efficient Electrocatalyst for Oxygen Reduction and Evolution Reactions, Catalysts. 8 (2018) 475. doi:10.3390/catal8100475.

[60] H.S. Jena, C. Krishnaraj, S. Parwaiz, F. Lecoeuvre, J. Schmidt, D. Pradhan, P. Van Der Voort, Illustrating the Role of Quaternary-N of BINOL Covalent Triazine-Based Frameworks in Oxygen Reduction and Hydrogen Evolution Reactions, ACS Appl. Mater. Interfaces. 12 (2020) 44689–44699. doi:10.1021/acsami.0c11381.

[61] L. Lai, J.R. Potts, D. Zhan, L. Wang, C.K. Poh, C. Tang, H. Gong, Z. Shen, J. Lin, R.S. Ruoff, Exploration of the active center structure of nitrogen-doped graphene-based catalysts for oxygen reduction reaction, Energy Environ. Sci. 5 (2012) 7936. doi:10.1039/c2ee21802j.

[62] K. Ai, Y. Liu, C. Ruan, L. Lu, G.M. Lu, Sp 2 C-Dominant N-Doped Carbon Sub-micrometer Spheres with a Tunable Size: A Versatile Platform for Highly Efficient Oxygen-Reduction Catalysts, Adv. Mater. 25 (2013) 998–1003. doi:10.1002/adma.201203923.

[63] H. Yang, X. Wang, S. Wang, P. Zhang, C. Xiao, H. Maleki Kheimeh Sari, J. Liu, J. Jia, B. Cao, J. Qin, W. Xiao, Z. Zhou, X. Li, Double boosting single atom Fe–N4 sites for high efficiency O2 and CO2 electroreduction, Carbon N. Y. 182 (2021) 109–116. doi:10.1016/j.carbon.2021.05.038.

[64] W. Xue, Q. Zhou, X. Cui, S. Jia, J. Zhang, Z. Lin, Metal–organic frameworks-derived heteroatom-doped carbon electrocatalysts for oxygen reduction reaction, Nano Energy. 86 (2021) 106073. doi:10.1016/j.nanoen.2021.106073.

[65] S. Chen, M. Cui, Z. Yin, J. Xiong, L. Mi, Y. Li, Single-Atom and Dual-Atom Electrocatalysts Derived from Metal Organic Frameworks: Current Progress and Perspectives, ChemSusChem. 14 (2021) 73–93. doi:10.1002/cssc.202002098.

[66] J. Ma, J. Li, R. Wang, Y. Yang, P. Yin, J. Mao, T. Ling, S. Qiao, Hierarchical porous S-doped Fe–N–C electrocatalyst for high-power-density zinc–air battery, Mater. Today Energy. 19 (2021) 100624. doi:10.1016/j.mtener.2020.100624.

[67] K. Wan, G.-F. Long, M.-Y. Liu, L. Du, Z.-X. Liang, P. Tsiakaras, Nitrogen-doped ordered mesoporous carbon: synthesis and active sites for electrocatalysis of oxygen reduction reaction, Appl. Catal. B. 165 (2015) 566–571. doi:10.1016/j.apcatb.2014.10.054.

[68] S.-H. Liu, S.-C. Chen, Well-dispersed FeN4 decorated mesoporous carbons for efficient oxygen reduction in acid media, Carbon N. Y. 105 (2016) 282–290. doi:10.1016/j.carbon.2016.04.042.

[69] J. Yang, D.-J. Liu, N.N. Kariuki, L.X. Chen, Aligned carbon nanotubes with built-in FeN 4 active sites for electrocatalytic reduction of oxygen, Chem. Commun. (2008) 329–331. doi:10.1039/B713096A.

[70] C. Domínguez, F.J. Pérez-Alonso, M.A. Salam, S.A. Al-Thabaiti, M.A. Peña, F.J. García-García, L. Barrio, S. Rojas, Repercussion of the carbon matrix for the activity and stability of Fe/N/C electrocatalysts for the oxygen reduction reaction, Appl. Catal. B. 183 (2016) 185–196. doi:10.1016/j.apcatb.2015.10.043.

[71] N. Cai, S. Xia, X. Zhang, Z. Meng, P. Bartocci, F. Fantozzi, Y. Chen, H. Chen, P.T. Williams, H. Yang, Preparation of Iron- and Nitrogen-Codoped Carbon Nanotubes from Waste Plastics Pyrolysis for the Oxygen Reduction Reaction, ChemSusChem. 13 (2020) 938–944. doi:10.1002/cssc.201903293.

[72] R. Hao, S. Gu, J. Chen, Z. Wang, Q. Gan, Z. Wang, Y. Huang, P. Liu, K. Zhang, K. Liu, C. Liu, Z. Lu, Microporous Fe–N4 cataysts derived from biomass aerogel for a high-performance Zn–air battery, Mater. Today Energy. 21 (2021) 100826. doi:10.1016/j.mtener.2021.100826.

[73] K. Liu, G. Wu, G. Wang, Role of Local Carbon Structure Surrounding FeN 4 Sites in Boosting the Catalytic Activity for Oxygen Reduction, J. Phys. Chem. C. 121 (2017) 11319–11324. doi:10.1021/acs.jpcc.7b00913.

[74] M. Xiao, Z. Xing, Z. Jin, C. Liu, J. Ge, J. Zhu, Y. Wang, X. Zhao, Z. Chen, Preferentially Engineering FeN 4 Edge Sites onto Graphitic Nanosheets for Highly Active and Durable Oxygen Electrocatalysis in Rechargeable Zn–Air Batteries, Adv. Mater. 32 (2020) 2004900. doi:10.1002/adma.202004900.

[75] J. Amaro-Gahete, J.A. Salatti-Dorado, A. Benítez, D. Esquivel, V. García-Caballero, M. López-Haro, J.J. Delgado, M. Cano, J.J. Giner-Casares, F.J. Romero-Salguero, Surface Diels–Alder adducts on multilayer graphene for the generation of edge-enriched single-atom FeN 4 sites for ORR and OER electrocatalysis, Sustain. Energy Fuels. 6 (2022) 1603–1615.

doi:10.1039/D2SE00004K.

[76] A. Benítez, D. Di Lecce, G.A. Elia, Á. Caballero, J. Morales, J. Hassoun, A Lithium-Ion Battery using a 3 D-Array Nanostructured Graphene-Sulfur Cathode and a Silicon Oxide-Based Anode, ChemSusChem. 11 (2018) 1512–1520. doi:10.1002/cssc.201800242.

[77] A.M. Kaczmarek, D. Esquivel, J. Ouwehand, P. Van Der Voort, F.J. Romero-Salguero, R. Van Deun, Temperature dependent NIR emitting lanthanide-PMO/silica hybrid materials, Dalton Trans. 46 (2017) 7878–7887. doi:10.1039/C7DT01620D.

[78] J. Amaro-Gahete, A.M. Kaczmarek, D. Esquivel, C. Jiménez-Sanchidrián, P. Van Der Voort, F.J. Romero-Salguero, Luminescent Graphene-Based Materials via Europium Complexation on Dipyridylpyridazine-Functionalized Graphene Sheets, Chem. – A Eur. J. 25 (2019) 6823–6830. doi:10.1002/chem.201900512.

[79] V. García-Caballero, H.K. Mohammed-Ibrahim, J.J. Giner-Casares, M. Cano, Influence of the synthesis route on the electrocatalytic performance for ORR of citrate-stabilized gold nanoparticles, Electrochem. Commun. 142 (2022) 107364. doi:10.1016/j.elecom.2022.107364.

[80] M. Ruben, J. Rojo, F.J. Romero-Salguero, L.H. Uppadine, J.-M. Lehn, Grid-Type Metal Ion Architectures: Functional Metallosupramolecular Arrays, Angew. Chem. Int. Ed. 43 (2004) 3644–3662. doi:10.1002/anie.200300636.

[81] D. Esquivel, A.M. Kaczmarek, C. Jiménez-Sanchidrián, R. Van Deun, F.J. Romero-Salguero, P. Van Der Voort, Eu 3+ @PMO: synthesis, characterization and luminescence properties, J. Mater. Chem. C. 3 (2015) 2909–2917. doi:10.1039/C4TC02553A.

[82] A.M. Kaczmarek, D. Esquivel, B. Laforce, L. Vincze, P. Van Der Voort, F.J. Romero-Salguero, R. Van Deun, Luminescent thermometer based on Eu3+/Tb3+-organic-functionalized mesoporous silica, Luminescence. 33 (2018) 567–573. doi:10.1002/BIO.3447.

[83] L.P. Wijesinghe, S.D. Perera, E. Larkin, G.M. Ó Máille, R. Conway-Kenny, B.S. Lankage, L. Wang, S.M. Draper, [2 + 2 + 2] cyclotrimerisation as a convenient route to 6N-doped nanographenes: a synthetic introduction to hexaazasuperbenzenes, RSC Adv. 7 (2017) 24163–24167. doi:10.1039/C7RA02648J.

[84] A. Sobkowiak, D. Naróg, D.T. Sawyer, Iron(III, II)-induced activation of

dioxygen for the oxygenation of cyclohexene and related unsaturated hydrocarbons, J. Mol. Catal. A Chem. 159 (2000) 247–256. doi:10.1016/S1381-1169(00)00198-9.

[85] D. Naróg, A. Szczepanik, A. Sobkowiak, Iron(II, III)-Catalyzed Oxidation of Limonene by Dioxygen, Catal. Lett. 120 (2008) 320–325. doi:10.1007/s10562-007-9290-7.

[86] D.W. Chang, H.-J. Choi, I.-Y. Jeon, J.-M. Seo, L. Dai, J.-B. Baek, Solvent-free mechanochemical reduction of graphene oxide, Carbon N. Y. 77 (2014) 501–507. doi:10.1016/j.carbon.2014.05.055.

[87] M. Simón, A. Benítez, A. Caballero, J. Morales, O. Vargas, Untreated Natural Graphite as a Graphene Source for High-Performance Li-Ion Batteries, Batteries. 4 (2018) 13. doi:10.3390/batteries4010013.

[88] A. Benítez, D. Di Lecce, Á. Caballero, J. Morales, E. Rodríguez-Castellón, J. Hassoun, Lithium sulfur battery exploiting material design and electrolyte chemistry: 3D graphene framework and diglyme solution, J. Power Sources. 397 (2018) 102–112. doi:10.1016/j.jpowsour.2018.07.002.

[89] J. Amaro-Gahete, A. Benítez, R. Otero, D. Esquivel, C. Jiménez-Sanchidrián, J. Morales, Á. Caballero, F. Romero-Salguero, A Comparative Study of Particle Size Distribution of Graphene Nanosheets Synthesized by an Ultrasound-Assisted Method, Nanomaterials. 9 (2019) 152. doi:10.3390/nano9020152.

[90] A. Benítez, A. Caballero, J. Morales, J. Hassoun, E. Rodríguez-Castellón, J. Canales-Vázquez, Physical activation of graphene: An effective, simple and clean procedure for obtaining microporous graphene for high-performance Li/S batteries, Nano Res. 12 (2019) 759–766. doi:10.1007/s12274-019-2282-2.

[91] A.C. Ferrari, J.C. Meyer, V. Scardaci, C. Casiraghi, M. Lazzeri, F. Mauri, S. Piscanec, D. Jiang, K.S. Novoselov, S. Roth, A.K. Geim, Raman Spectrum of Graphene and Graphene Layers, Phys. Rev. Lett. 97 (2006) 187401. doi:10.1103/PhysRevLett.97.187401.

[92] A.C. Ferrari, Raman spectroscopy of graphene and graphite: Disorder, electron–phonon coupling, doping and nonadiabatic effects, Solid State Commun. 143 (2007) 47–57. doi:10.1016/j.ssc.2007.03.052.

[93] H.-W. Liang, W. Wei, Z.-S. Wu, X. Feng, K. Müllen, Mesoporous Metal–Nitrogen-Doped Carbon Electrocatalysts for Highly Efficient Oxygen Reduction Reaction, J. Am. Chem. Soc. 135 (2013) 16002–16005. doi:10.1021/ja407552k.

[94] J. Zhang, D. He, H. Su, X. Chen, M. Pan, S. Mu, Porous polyaniline-derived FeN x C/C catalysts with high activity and stability towards oxygen reduction reaction using ferric chloride both as an oxidant and iron source, J. Mater. Chem. A. 2 (2014) 1242–1246. doi:10.1039/C3TA14065B.

[95] D. Lyu, Y.B. Mollamahale, S. Huang, P. Zhu, X. Zhang, Y. Du, S. Wang, M. Qing, Z.Q. Tian, P.K. Shen, Ultra-high surface area graphitic Fe-N-C nanospheres with single-atom iron sites as highly efficient non-precious metal bifunctional catalysts towards oxygen redox reactions, J. Catal. 368 (2018) 279–290. doi:10.1016/j.jcat.2018.10.025.

[96] B. Gupta, N. Kumar, K. Panda, S. Dash, A.K. Tyagi, Energy efficient reduced graphene oxide additives: Mechanism of effective lubrication and antiwear properties, Sci. Rep. 6 (2016) 18372. doi:10.1038/srep18372.

[97] S. Joshi, R. Siddiqui, P. Sharma, R. Kumar, G. Verma, A. Saini, Green synthesis of peptide functionalized reduced graphene oxide (rGO) nano bioconjugate with enhanced antibacterial activity, Sci. Rep. 10 (2020) 9441. doi:10.1038/s41598-020-66230-3.

[98] Y. Li, G. Louarn, P.-H. Aubert, V. Alain-Rizzo, L. Galmiche, P. Audebert, F. Miomandre, Polypyrrole-modified graphene sheet nanocomposites as new efficient materials for supercapacitors, Carbon N. Y. 105 (2016) 510–520. doi:10.1016/j.carbon.2016.04.067.

[99] Y. Zhao, W. Wang, J. Li, F. Wang, X. Zheng, H. Yun, W. Zhao, X. Dong, FeCl 3 /pyridine: dual-activation in opening of epoxide with carboxylic acid under solvent free condition, Tetrahedron Lett. 54 (2013) 5849–5852. doi:10.1016/j.tetlet.2013.08.074.

[100] S. Biniak, G. Szymański, J. Siedlewski, A. Świątkowski, The characterization of activated carbons with oxygen and nitrogen surface groups, Carbon N. Y. 35 (1997) 1799–1810. doi:10.1016/S0008-6223(97)00096-1.

[101] S. Maldonado, S. Morin, K.J. Stevenson, Structure, composition, and chemical reactivity of carbon nanotubes by selective nitrogen doping, Carbon N. Y. 44 (2006) 1429–1437. doi:10.1016/j.carbon.2005.11.027.

[102] T. Chen, J. Wu, C. Zhu, Z. Liu, W. Zhou, C. Zhu, C. Guan, G. Fang, Rational design of iron single atom anchored on nitrogen doped carbon as a high-performance electrocatalyst for all-solid-state flexible zinc-air batteries, Chem. Eng. J. 405 (2021) 125956. doi:10.1016/J.CEJ.2020.125956.

[103] Y.-L. Liu, X.-Y. Xu, C.-X. Shi, X.-W. Ye, P.-C. Sun, T.-H. Chen, Iron–nitrogen co-doped hierarchically mesoporous carbon spheres as highly efficient electrocatalysts for the oxygen reduction reaction, RSC Adv. 7 (2017) 8879–8885. doi:10.1039/C6RA26917F.

[104] B.J. Kim, D.U. Lee, J. Wu, D. Higgins, A. Yu, Z. Chen, Iron- and Nitrogen-Functionalized Graphene Nanosheet and Nanoshell Composites as a Highly Active Electrocatalyst for Oxygen Reduction Reaction, J. Phys. Chem. C. 117 (2013) 26501–26508. doi:10.1021/jp410014a.

[105] H. Tan, J. Tang, J. Kim, Y.V. Kaneti, Y.-M. Kang, Y. Sugahara, Y. Yamauchi, Rational design and construction of nanoporous iron- and nitrogen-doped carbon electrocatalysts for oxygen reduction reaction, J. Mater. Chem. A. 7 (2019) 1380–1393. doi:10.1039/C8TA08870E.

[106] Y. Chen, S. Xie, L. Li, J. Fan, Q. Li, Y. Min, Q. Xu, Highly accessible sites of Fe-N on biomass-derived N, P co-doped hierarchical porous carbon for oxygen reduction reaction, J. Nanoparticle Res. 23 (2021) 68. doi:10.1007/s11051-021-05176-7.

[107] Y. Chen, X. Kong, Y. Wang, H. Ye, J. Gao, Y. Qiu, S. Wang, W. Zhao, Y. Wang, J. Zhou, Q. Yuan, A binary single atom Fe3C|Fe N C catalyst by an atomic fence evaporation strategy for high performance ORR/OER and flexible Zinc-air battery, Chem. Eng. J. 454 (2023) 140512. doi:10.1016/j.cej.2022.140512.